Shock Waves (2010) 20:147–162
DOI 10.1007/s00193-009-0236-4

ORIGINAL ARTICLE

Numerical study of blast characteristics from detonation of homogeneous explosives

Kaushik Balakrishnan · Franklin Genin · Doug V. Nance · Suresh Menon

Received: 7 February 2009 / Revised: 15 September 2009 / Accepted: 13 October 2009 / Published online: 25 October 2009

Abstract A new robust numerical methodology is used to investigate the propagation of blast waves from homogeneous explosives. The gas-phase governing equations are solved using a hybrid solver that combines a higher-order shock capturing scheme with a low-dissipation central scheme. Explosives of interest include Nitromethane, Trinitrotoluene, and High-Melting Explosive. The shock overpressure and total impulse are estimated at different radial locations and compared for the different explosives. An empirical scaling correlation is presented for the shock overpressure, incident positive phase pressure impulse, and total impulse. The role of hydrodynamic instabilities to the blast effects of explosives is also investigated in three dimensions, and significant mixing between the detonation products and air is observed. This mixing results in afterburn, which is found to augment the impulse characteristics of explosives. Furthermore, the impulse characteristics are also observed to be three-dimensional in the region of the mixing layer. This paper highlights that while some blast features can be successfully predicted from simple one-dimensional studies, the growth of hydrodynamic instabilities and the impulsive loading of homogeneous explosives require robust three-dimensional investigation.

Communicated by S. Dorofeev.

K. Balakrishnan · F. Genin · S. Menon (✉)
School of Aerospace Engineering, Georgia Institute of Technology, Atlanta, GA 30332-0150, USA
e-mail: suresh.menon@aerospace.gatech.edu

D. V. Nance
Air Force Research Laboratory, Eglin Air Force Base, FL 32542-6810, USA

Keywords Detonation · Blast wave · Overpressure · Impulse · Instability

PACS 82.33.Vx

1 Introduction

Explosives have been in use for well over a century in varying applications, such as military armaments, commercial blasting, to extinguish fires, etc. Many different types of explosives are in use with different strengths and signatures, and these characteristics determine their application. A proper understanding of the physics that govern their behavior is essential to the research and development of the next generation of explosives with tailored performance characteristics. Experimental studies are expensive and hazardous, and data collection cumbersome. Computational simulations can therefore, play a vital role in investigating the governing physics provided proper conditions can be simulated.

When an explosive charge is detonated, a detonation wave propagates through the explosive material. As this detonation wave reaches the outer surface of the explosive charge, a blast wave propagates outwards, and a rarefaction wave inwards, forcing an outward acceleration of the detonation product gases. The contact surface between the detonation products and the shock-compressed air is swept outwards, and is hydrodynamically unstable to perturbations due to the large density gradients across it. At the vicinity of the contact surface, a slight distortion of the equilibrium between the heavy and the light fluids on either side can grow, resulting in Rayleigh-Taylor [1] instabilities. At the same time, the inward moving rarefaction wave overexpands the flow, and this gives rise to a secondary shock [2]. This secondary shock is initially weak, and is swept outwards by

the detonation product gases. During this time, the secondary shock strengthens, and subsequently implodes inwards. When the secondary shock reflects from the origin, it propagates outwards and interacts with the Rayleigh-Taylor structures, giving rise to further growth of these hydrodynamic instabilities, this time in the form of Richtmyer-Meshkov instabilities [3]. During this interaction, a second rarefaction wave can also be generated, moving inwards. This rarefaction wave, like its predecessor, can overexpand the flow, giving rise to a tertiary shock. This process of subsequent shock formation repeats until most of the energy of the detonation product gases is expended as kinetic energy of the outward flow.

The scale of the instability growth is critical to the mixing process between the detonation products and the shock-compressed air. If the initial surface of the charge is rough, the initial instabilities start to grow from that scale itself [4]. On the other hand, if the initial charge surface is hydrodynamically smooth, the instabilities start to grow from molecular scales at a rate predicted by the linear stability theory. In both scenarios, the instabilities grow to macroscopic scales and form a turbulent mixing layer. The resulting inevitable mixing between the core detonation products and the outer air results in afterburn, which occurs at a rate controlled by turbulent mixing, rather than by molecular diffusion [5]. The role of these hydrodynamic instabilities is significant, especially for thermobaric explosives such as TNT. The term "thermobaric" is used to describe explosives that can afterburn, a phenomenon owing to the mixing between the carbon in the detonation products and the ambient oxygen, which occurs at time scales several orders of magnitude larger than the detonation time scales. This mixing is augmented by hydrodynamic instabilities and turbulence, and cannot be accurately predicted from one-dimensional (1D) studies. On the other hand, 1D studies are simple to undertake, and are useful to understand some of the detonation features.

Several one-dimensional studies have been carried out in the past to study blast waves. Based on available experimental data, scaling laws for blast wave decay and impulse have been reported in the past [6]. The earliest scaling law of Hopkinson (1915) [6] suggested that blast waves from two different charges of different weights, but of the same explosive, would have the same strength at the same scaled distance. This scaled distance (units: $\mathrm{m\,kg^{-1/3}}$) is given by $r/W^{1/3}$, where r denotes the distance from the explosive in m, and W is the weight of the explosive in the charge in kg. This scaling law forms the basis of many scaling laws proposed for explosives in the later years. For example, the Sachs scaling law (1944) [6] is a modification of the Hopkinson law to account for atmospheric conditions, and the scaled distance is given by $r\,{p_o}^{1/3}/E^{1/3}$, where p_o is the ambient pressure in bar, and E is the detonation energy from the charge in Joules. This scaling law assumes that air behaves as a perfect gas, and that the effects of viscosity and gravity are negligible [6]. Another widely used scaling is the TNT equivalence, which has been reported for a few commercial blasting explosives [7,8]. However, experimental studies [9] on gram-range explosive charges have shown that a single TNT equivalence value is insufficient to represent the overall explosive strength. Thus, several such scaling laws and parameters exist to characterize the behavior of explosives, assuming one-dimensional post-detonation behavior of the explosive.

Numerical studies on blast effects from explosives have also been undertaken. Brode [2] undertook one of the first numerical studies of an explosive charge (TNT) using a one-dimensional assumption and presented overpressure impulse. Numerical study of bursting spheres was carried out by Vanderstraeten et al. [10], and they proposed an empirical model to estimate the peak overpressure as a function of the energy scaled distance. They also presented an empirical expression for the explosive efficiency as a function of the contact surface velocity. A general discussion of the phenomena involved in the estimation of blast loading from three explosive scenarios, i.e., from atomic weapons, conventional high explosives, and unconfined vapor cloud explosions on above-ground structures was reported by Beshara [11]. In this study, loading was characterized from dynamic pressure and reflected overpressure. A comparison of the several scaling laws proposed for TNT has been reported [12] with simple curve-fit expressions for the blast wave parameters.

All the above-noted studies were based on a one-dimensional assumption of the blast effects from explosive charges. In a recent study [13], the effect of TNT blast characteristics on nearby structures was studied in three dimensions. However, this study did not include the effects of hydrodynamic instabilities and turbulence, which can enhance mixing between the detonation products and the shock compressed air. We will show in this paper that these mixing characteristics are significant to the afterburn, and to the impulsive aspects of explosives.

The physics of hydrodynamic instabilities have been studied in detail but not widely applied to explosives (see for instance [14,15] and the references therein). The growth of instabilities in the contact surface of an explosive fireball was first reported by Anisimov and Zeldovich [16,17]. They identified two limiting cases, i.e., when the length scale of the instability is much less than the distance between the primary and secondary shock (they refer to it as free Rayleigh-Taylor turbulence), and when the scale of the instability is of the same order. They identified that the position of the secondary shock decides the spatial scale of the initial Taylor modes, and hence, the rate of mixing between the detonation products and the shock-compressed air. Kuhl et al. [5,18], in a series of papers, performed a numerical investigation of

the growth of hydrodynamic instabilities in explosives and its significance to the afterburn of the detonation products using an adaptive mesh refinement (AMR) technique. Four different regimes/phases were identified by the authors: (i) blast wave, (ii) implosion, (iii) re-shock, and (iv) asymptotic mixing [5]. They reported that while the mean kinetic energy decays rapidly, the fluctuating component asymptotes to a constant value at late times, thereby highlighting the turbulent nature of the mixing region. Baroclinic torque effect (misaligned pressure and density gradients) was observed to cause vorticity in the mixing region, which decays at late times. In [18], the authors reported that most (∼90%) of the afterburn of the detonation products occurs in the asymptotic mixing phase, due to the merging of vortex rings and the accompanying wrinkling of the exothermic surface.

These past studies have highlighted that the growth of hydrodynamic instabilities in an explosive charge results in enhanced mixing between the detonation products and the outer air, resulting in afterburning exothermicity. However, these three-dimensional studies have not directly addressed the role of hydrodynamic instabilities and the concomitant afterburn energy on the impulsive aspects of explosive charges. If the afterburn energy release is fast enough, its contribution to the impulsive loading can be significant. On the other hand, if the afterburn energy release is slow, the impulsive loading will be close to the 1D predictions. Thus, the mixing and afterburn phenomena are critical to the impulsive loading estimation from explosives, which has not been addressed in the aforementioned studies. This is one of the primary motivations in the current research effort.

This study is undertaken with two main objectives: (1) to characterize the explosive behavior of a few commercial explosives, and (2) to understand the effect of hydrodynamic instabilities on the blast effects and impulsive loading from explosives. To meet the first objective, three explosives are considered, i.e., Nitromethane (NM), Trinitrotoluene (TNT) and High-Melting Explosive (HMX), and their blast overpressure, trajectory, and impulsive loading are studied. Scaling laws are obtained for these three explosives, using which, a generalized scaling law is proposed, applicable for any explosive with a prescribed detonation energy, useful for the design of the next generation of explosives. To meet the second objective, a spherical TNT charge is studied with Gaussianly random perturbations added in the vicinity of the outer surface of the charge. The ensuing hydrodynamic instability growth is studied and its role on the blast effects is investigated.

This paper is organized as follows. In Sect. 2, the numerical formulation of the present study is described. In Sect. 3, we present the numerical methodology used in the study. In Sect. 4, the results obtained are presented and discussed, followed by the conclusions in Sect. 5.

2 Formulation

The simulations are conducted using the unsteady, compressible, reacting, multispecies Navier-Stokes equations, and are summarized as

$$\frac{\partial}{\partial t}\begin{bmatrix}\rho\\ \rho u_i\\ \rho E\\ \rho Y_k\end{bmatrix}+\frac{\partial}{\partial x_j}\begin{bmatrix}\rho u_j\\ \rho u_i u_j+p\delta_{ij}-\tau_{ij}\\ (\rho E+p)\,u_j-u_i\tau_{ji}+q_j\\ \rho Y_k\left(u_j+V_{j,k}\right)\end{bmatrix}=\begin{bmatrix}0\\0\\0\\ \dot{\omega}_k\end{bmatrix}-\frac{\eta}{x_j}\begin{bmatrix}\rho u_j,\\ \rho u_j u_j,\\ (\rho E+p)\,u_j,\\ \rho Y_k u_j,\end{bmatrix} \tag{1}$$

where ρ denotes the density, u_i is the i-th component of velocity, E is the specific total energy given by the sum of the internal (e) and the kinetic energy, $e+\frac{1}{2}u_i u_i$, p is the pressure, and Y_k, the mass fraction of the k-th species. The chemical production of the k-th species is represented by $\dot{\omega}_k$. Denoting the total number of chemical species as N_s, the index k in the species equation varies as $k=1,\ldots,N_s$. For one-dimensional simulations, x_j can be replaced by the radial coordinate r, and the last matrix on the right side of (1) (which is zero for multidimensional cases) is used to account for the geometric source term due to the planar/cylindrical/spherical nature of the problem, with $\eta=0$, 1 and 2, for planar, cylindrical, and spherical coordinate systems, respectively. The stress tensor is denoted by τ_{ij}, j-direction heat flux by q_j, and the j-component diffusion velocity by $V_{j,k}$. The stress tensor is given by

$$\tau_{ij}=\mu\left(\frac{\partial u_i}{\partial x_j}+\frac{\partial u_j}{\partial x_i}\right), \tag{2}$$

where μ represents the viscosity of the gas phase. The heat flux is given by

$$q_j=-\kappa\frac{\partial T}{\partial x_j}+\rho\sum_{k=1}^{N_s}h_k Y_k V_{j,k}, \tag{3}$$

where T denotes the temperature, κ, the thermal conductivity, and h_k, the specific enthalpy for the k-th species. The diffusion velocity is computed from Fick's law, i.e., $V_{j,k}=-D_k/Y_k\left(\partial Y_k/\partial x_j\right)$, where D_k denotes the diffusion coefficient of the k-th species, obtained from unity Schmidt number assumption. The diffusion terms are neglected for the one-dimensional simulations, since the convective time-scales are smaller than the diffusive time-scales in the current study.

The chemical source term, $\dot{\omega}_k$ that arises due to combustion/afterburn has to be determined. Due to the very high temperatures and pressures involved in the problem under study, the conventional finite-rate Arrhenius kinetics based reaction rates are probably not applicable, as these curve-fit expressions are based on very different flow conditions,

i.e., lower temperatures and pressures. Thus, for the present study, the chemical rates are obtained on the assumption of infinite chemistry, which is generally used to model afterburn in explosives (see for instance [18]). Here, the underlying assumption is that the chemical kinetic time scale is zero, i.e., the problem is reduced to a "mixing-controlled" combustion process rather than a "chemically controlled" process [5]. The two steps involved in the chemistry are given by

$$\begin{aligned} C + \frac{1}{2} O_2 &\rightarrow CO, \\ CO + \frac{1}{2} O_2 &\rightarrow CO_2. \end{aligned} \tag{4}$$

Here, the species are assumed to exist in the gaseous phase. At each time step, the fuel (C or CO) and oxygen concentrations are compared in each finite volume cell, and, based on the stoichiometric ratio, it is deduced whether the cell corresponds to a fuel-lean or fuel-rich scenario. For fuel-lean cells, all the fuel is consumed instantaneously, and the amount of oxygen to be involved in the reaction is determined from stoichiometry. The same procedure is repeated for fuel-rich cells, with all the oxygen consumed, and the amount of fuel involved determined from stoichiometry.

To establish a relation between the thermodynamic variables, an appropriate equation of state is needed. The perfect gas equation of state is given by $p = \rho RT$, where R and T denote, respectively, the gas constant and temperature of the gas. The speed of sound (a) for a perfect gas is given by $a^2 = \gamma p/\rho$, where γ denotes the ratio of specific heats of the gas. For a calorically perfect gas, γ is a constant, while for a thermally perfect gas, γ is assumed to vary with temperature. Since the detonation products are at very high pressures and densities, the use of a perfect gas fails to accurately predict the blast characteristics, as we will later show. A real gas model that accounts for the dependence of the internal energy on both pressure and density is thus essential. To this end, the detonation products for many explosives are modeled by using the Jones-Wilkins-Lee (JWL) equation of state [19,20] to account for real gas behavior and is given by

$$\begin{aligned} p(\rho, e) = A \left[1 - \frac{\omega\rho}{R_1\rho_o}\right] \exp\left(-\frac{R_1\rho_o}{\rho}\right) \\ + B \left[1 - \frac{\omega\rho}{R_2\rho_o}\right] \exp\left(-\frac{R_2\rho_o}{\rho}\right) + \omega\rho\,(e - e_0)\,, \end{aligned} \tag{5}$$

where A, B, R_1, R_2, ρ_o, and ω are constants for an explosive and e_0 denotes a reference internal energy. These constants for several explosives are documented [20]. Like many equations of state, the JWL equation of state is similar in mathematical form to the Mie-Gruneisen equation of state, i.e., it can be represented as $p(\rho, e) = f(\rho) + \omega\rho e$, where $f(\rho)$ is a function of ρ, and ω is a constant. When $f(\rho) = 0$ and $\omega = \gamma - 1$, the Mie-Gruneisen equation of state reduces to the perfect gas. The ambient air can be modeled by the Van Der Waal's equation of state [21], given by

$$\left(p + a\frac{n^2}{V^2}\right)(V - nb) = nRT, \tag{6}$$

where a and b are constants, n denotes the number of moles, and V, the volume of the gas. When a combination of equations of state are used, an additional closure is essential. To this end, the gas mixture can be assumed to be either in thermal or mechanical equilibrium.

Another widely used equation of state is the Noble-Abel equation of state [22], given by

$$p = \frac{\rho RT}{1 - An}, \tag{7}$$

where R denotes the gas constant, n, the number of moles per unit volume, and A, an empirical constant. The empirical constant, A, is determined from two criterions: (1) ensuring the term $1 - An$ always remains positive; (2) from apriori knowledge of the blast wave overpressure. Furthermore, to obtain the enthalpy of the gas, the specific heat capacities (C_p) are used, and are assumed to vary with temperature by means of polynomial curve-fits [23]. Finally, the frozen speed of sound for a real gas [24] is obtained as

$$a^2 = \left(\frac{\partial p}{\partial \rho}\right)_e + \frac{p}{\rho^2}\left(\frac{\partial p}{\partial e}\right)_\rho. \tag{8}$$

3 Numerical methodology

3.1 Algorithm

The problem under study is multiscale in nature, i.e., involves shocks, as well as hydrodynamic instabilities. Here, a hybrid numerical method capable of accounting for both phenomena is employed. The governing equations are solved using a finite-volume formulation in which the propagating shocks and discontinuities are captured using a higher order flux difference splitting method, and the resolution of the vortical/turbulent structures in the flow is performed by employing a low-dissipation central scheme. The flux difference splitting method uses the Monotone Upstream-centered Schemes for Conservation Laws (MUSCL) reconstruction approach along with a Monotonized Central limiter [25]. An approximate Riemann solver is then used to solve for the fluxes at the interface. A hybrid Riemann solver that combines the HLLC method of Toro [26] is the base solver, with the HLL approximate solver [26] within the shock thickness in directions transverse to the high-pressure gradient directions is used. This hybrid solver retains the accuracy of the HLLC method, and dampens spurious instabilities. This upwind scheme is used only in regions of strong discontinuities (shocks, sharp rarefactions, contact discontinuities), and

regions dominated by vortical structures and/or turbulent structures are resolved using a second-order accurate central scheme [27]. A smoothness parameter is defined and used to switch between the central scheme to the upwind method. Time-integration is performed using a predictor-corrector method, leading to a second-order, time-accurate, explicit temporal resolution.

3.2 Modeling the detonation initial conditions

To carry out the detonation studies, the initial conditions from the condensed phase detonation must be obtained. To simulate the condensed phase detonation, some hydrocodes are equipped with a programmed burn (PB) algorithm to obtain the initial detonation profiles. However, it is known that PB fails to resolve the detonation reaction zone and cannot capture the Von Neumann spike [28]. Another easy initialization could be to use a Constant Volume Explosion (CVE) [29]. In a CVE, the initial charge is initialized with a high pressure that is determined from chemistry relations. This procedure, although simple, is not physical, as the total detonation energy is equally distributed within the charge. To overcome these deficiencies, we employ the Gas-Interpolated-Solid Stewart-Prasad-Asay (GISPA) method to model the initial detonation process [30]. This method permits a time-accurate simulation of detonation from the time of the initial shock through the completion of the explosive burn. GISPA also captures the reaction zone and the Von Neumann spike. GISPA solutions are commonly used to validate current detonation physics models such as Detonation Shock Dynamics (DSD) [30]. Moreover, the quality of these solutions is suitable for the design of modern explosive components [31].

The GISPA method is based on the one-dimensional reactive Euler equations, summarized in (1), with the only difference being that we do not consider multispecies; rather we consider a single reaction progress variable, λ, which determines the degree of the detonation. The reaction rate expression for the detonation process is non-specific, since it takes on different forms for different explosives. Proper equations of state for both the condensed explosive (liquid or solid) and the detonation products (gases) must be included to solve the governing equations [30]. Here, we use the Hayes equation of state for the condensed explosive [32] and the JWL equation of state for the product gases [20]. The GISPA method utilizes mixture-based quantities [33], and the mixture equation of state is defined as $e(\rho, p, \lambda) = (1-\lambda)e(\rho_s, p) + \lambda e(\rho, p)$ (the subscript s is used to denote the condensed explosive). The governing equations are solved by flux-difference splitting using the Glaister's version of the Roe scheme for equations of state of the form $e = e(\rho, p, \lambda)$ with the exact calculation of pressure derivatives [24]. We apply MUSCL extrapolation to the primitive variables and employ a non-linear limiter to restore monotonicity to the extrapolated variables.

Extensive validation studies have been performed and a representative case is discussed here. A basic detonation problem used for validation applies the detonation equations of state to a calorically perfect gas [30]. The specific internal energy for the detonation products has the form $e(\rho, p) = \frac{p}{\rho(\gamma-1)} - Q$. For this equation of state, the detonation Hugoniots are well behaved, and the computed solution can be compared to an exact solution. Based upon the initial conditions provided in Xu et al. [30], the predicted solutions for pressure and gas velocity are shown in Fig. 1, and the agreement between the numerical and the exact solutions is quite good. Both the speed and the shape of the detonation, and the Taylor waves are captured quite accurately.

We can also validate our detonation algorithms for condensed explosive materials that possess equation of state and reaction rate data. Of particular interest in this study is the liquid explosive NM used in the experiments performed by Zhang et al. [29]. Data for both Hayes and JWL equations of state for NM, and a suitable reaction rate expression are available [19]. For verification, we compare the macroscopic parameters such as the Chapman-Jouguet (CJ) conditions and detonation velocity [19], and base our validation on the plane wave detonation solution. It is necessary to estimate the location of the end of the reaction zone in order to fix the CJ

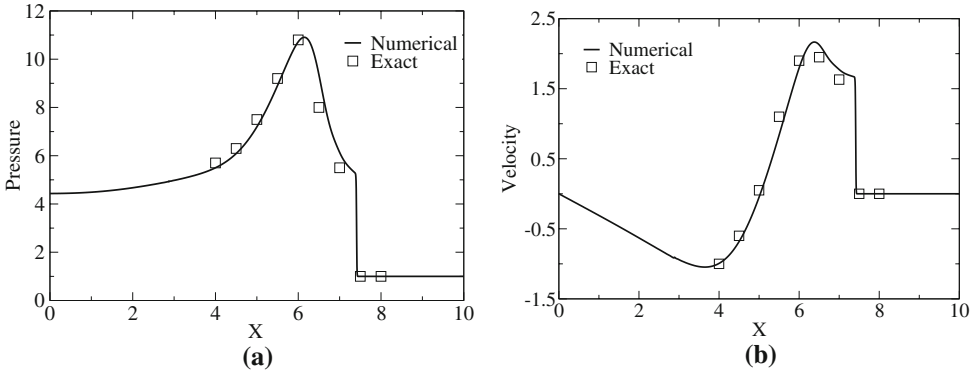

Fig. 1 Detonation wave profile (**a**) pressure (non-dimensional) and (**b**) velocity (non-dimensional) for the calorically perfect gas equation of state

Table 1 Detonation programming validation data for nitromethane: P_{CJ} - CJ pressure, u_{CJ} - CJ velocity, D - detonation velocity

Property	Numerical	Empirical	% Difference
P_{CJ} (Pa)	0.138×10^{11}	0.125×10^{11}	10.4
u_{CJ} (m/s)	2,030	1,765	15.0
D (m/s)	6,337	6,280	−0.9

point and its properties. The computed CJ parameters (pressure, gas velocity, and detonation wave speed) for NM are provided in Table 1 along with the empirical values. The comparisons with experimental data are good, especially when considering the level of variation in the measurement procedures. For NM, and other explosives, e.g., TNT, and HMX, the detonation pressure and velocity profiles as the detonation wave reaches the outer end of a 11.8 cm dia. charge are shown in Fig. 2.

The detonation initialization based on GISPA is compared with the CVE method for a 11.8 cm dia. TNT charge. Specifically, we compare the blast wave overpressure and impulsive loading (to be defined in Sect. 4.1) for the two different detonation initialization procedures. A one-dimensional simulation is undertaken with 5,000 grid points, and is found to be sufficient based on a grid independence study, not shown here for brevity. The shock overpressure and impulse are shown in Fig. 3 for the two different initializations. The shock wave overpressure is under-predicted by the CVE initialization in the near-field, but approximately matches the prediction by the GISPA initialization in the far-field. Furthermore, the impulse prediction from CVE is about 15% lower than the GISPA. In the CVE initialization, the pressure is assumed uniform (8.12 GPa for TNT [34]) and zero velocity within the charge, resulting in an equally distributed initial energy. On the other hand, in the GISPA method, the initial profile represents a true detonation process; thus, more energy is concentrated in the vicinity of the leading blast wave.

3.3 Sector grid approach

For the three-dimensional studies of the spherical blast wave problem, we use a spherical sector grid approach. This approach considers only a part of a sphere, i.e., a spherical sector centered about the equator. The main advantage of using only a part of the sphere is the reduction in computational simulation time. This approach has been used very recently to study turbulent mixing in spherical implosions [35]. However, one of the problems associated with this approach is the singularity at the origin. For a sector grid, the finite-volume scheme fails near the origin, as the surface area tends to zero. To overcome this singularity at the origin, a few options exist. First, a small spherical ball can be assumed at the origin, so that the finite volume scheme is used beyond a small radial sector around the origin. The size of the spherical ball must be small when compared to the initial charge size, so that the simulated charge contains almost the same amount (e.g., >99.9%) of the high explosive as the real charge. A similar approach has been used to study heat transfer in a cone, where a small hemisphere was used around the origin to eliminate the singularity [36].

Another option is to enforce a 1D radial region close to the origin where the flow is strictly radial, starting from zero radial velocity at the origin [35]. The flow variables are evaluated in this 1D region, and the velocity of the outermost 1D radial region provides the boundary condition for the innermost 3D finite volume cell. In the spherical ball approach, no convective flux is allowed across the innermost cell interface, which is not the case in the latter. In both approaches, the main defect is the lack of three-dimensionality in the vicinity of the origin, i.e., if a vortex reaches the origin from one quadrant, it is bounced back to the same quadrant. However, for the problem under study (and in [35]), the region of dominant turbulence/vortical structures occurs primarily in the mixing layer and not near the origin. Thus, both these approaches can be used for the problem under study. The 1D simplified approach of [35] is essential when the 1D zone is a comparable fraction of the domain size. However, in the present

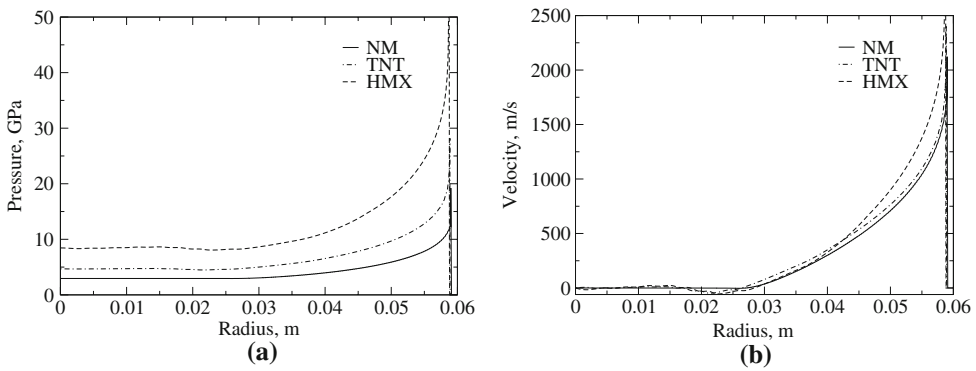

Fig. 2 Initial profiles for the homogeneous 11.8 cm dia NM/TNT/HMX charges (**a**) pressure; (**b**) velocity

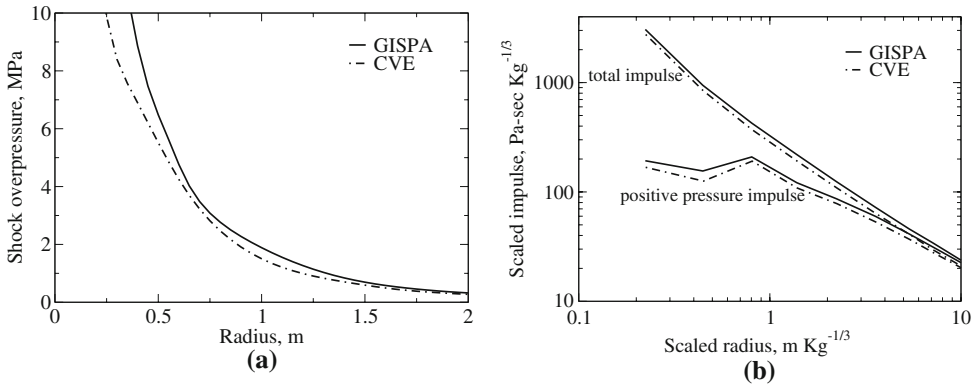

Fig. 3 Comparison of shock overpressure and impulse for initializations based on GISPA (Sect. 3.2) and constant volume explosion (CVE) (**a**) overpressure; (**b**) impulse

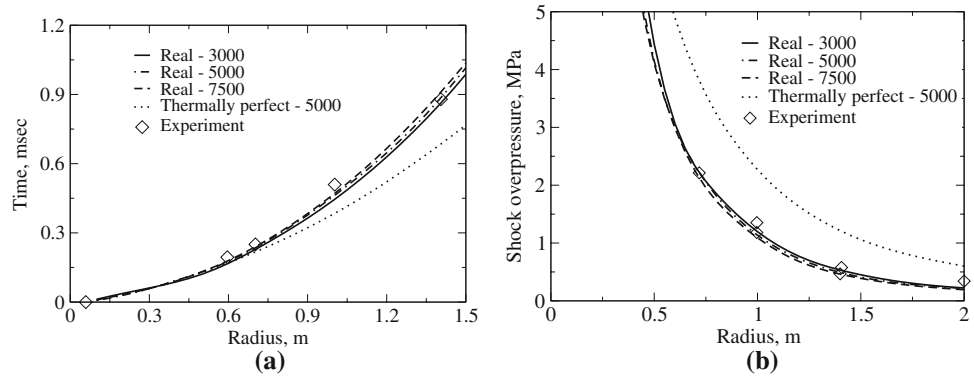

Fig. 4 Blast wave from a Nitromethane charge (**a**) trajectory; (**b**) overpressure. Experimental data from [29]. The *numbers* denote the number of grid points used for the one-dimensional grid. Real: real gas assumption, Thermally perfect: thermally perfect gas assumption

study, the 1D zone is assumed to be very small ($\sim$ 2.5 mm), and thus, the spherical ball assumption suffices.

4 Results and discussion

The simulation code is a well-established DNS/LES solver capable of handling reactive, turbulent, multiphase, and high-speed flows [37]; we undertake a DNS for the present study. Many canonical tests have been carried out in one-dimension as well as in three-dimensions to evaluate the accuracy of the solver, and some of the critical ones are summarized in Appendix A.

The blast from a 11.8 cm dia. spherical NM charge is simulated using the one-dimensional approach with the geometric source terms in (1). To study grid independence, various grids of sizes 3,000, 5,000, and 7,500 are used to simulate a 12-m-long domain, and the blast wave trajectory and overpressure are shown in Fig. 4 along with the experimental data of [29]. Grid convergence is achieved for the range of grids, and therefore, we use 5,000 grid points for all the one-dimensional studies. Also shown in the figure are the results using the thermally perfect gas model. It is clear that the thermally perfect gas assumption significantly overpredicts the shock speed and the overpressure, thus demonstrating the need to employ a proper real gas equation of state.

4.1 Blast wave and impulsive loading

To simulate blast wave propagation, the 1D approach is used with 5,000 grid points in a 12 m long domain, and the detonation profiles are initialized corresponding to a 11.8 cm dia. initial charge. Some relevant detonation characteristics for the various explosives are summarized in Table 2. For these explosives, the primary and secondary shock trajectories and the shock overpressure are shown in Fig. 5. The primary shock is faster for HMX, followed by TNT and last, NM, consistent with the order of the mass of the high explosive (and total detonation energy) in each charge. The secondary shock is observed to travel a farther distance during its initial outward movement in the same order for the three explosives, i.e., by 9 cm farther for TNT than NM, and by 5 cm for HMX than TNT. The strength of the primary shock, i.e.,

Table 2 Properties of the three explosives considered: P_{CJ} - CJ pressure, ρ_o - initial density, D - detonation velocity, E - detonation energy

Explosive	P_{CJ} (GPa)	ρ_o (kg/m^3)	D (Km/s)	E (MJ/kg)
NM (CH_3NO_2)	12.5	1,128	6.28	4.35
TNT ($C_7H_5N_3O_6$)	21.0	1,630	6.93	4.84
HMX ($C_4H_8N_8O_8$)	42.0	1,891	9.11	5.86

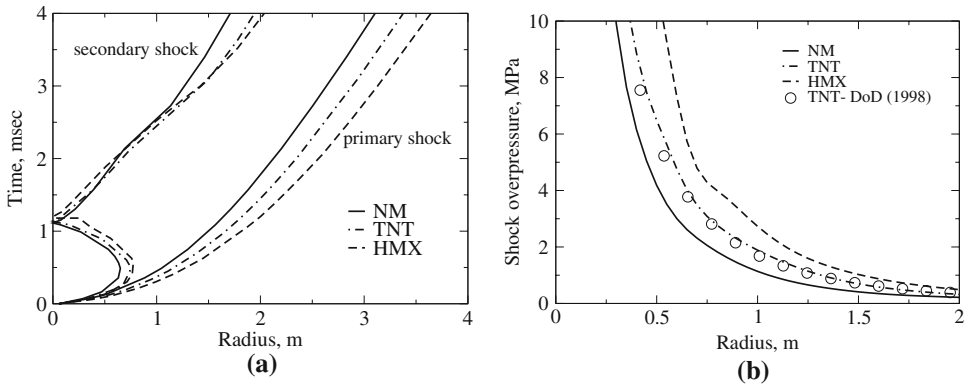

Fig. 5 Blast wave from charges containing the same volume of the high explosive (**a**) primary and secondary shock trajectories; (**b**) overpressure. [38]

the shock overpressure also increases with the total detonation energy. For comparison, the blast overpressure of TNT based on a curve-fit expression from [38] is also shown in the figure, and is observed to be in reasonable agreement with our prediction.

The total impulsive loading from a homogeneous charge is obtained at different radial locations for the three explosives considered. We estimate the impulsive loading on a 'virtual wall,' i.e., without the consideration of blast wave reflection/diffraction. Under this assumption, the total deliverable impulse will be due to gas pressure and momentum flux (dynamic pressure). Thus, we define the total impulse as

$$I = \int_0^\infty (p - p_o)_{p>p_o} \mathrm{d}t + \int_0^\infty \frac{1}{2}\rho u^2 \mathrm{d}t, \tag{9}$$

where p_o denotes the ambient pressure. For a real wall/ structure, the drag coefficient between the flow and the wall/structure has to be included in the impulse term due to flow momentum.

Scaling laws have been provided for the incident positive phase pressure impulse [8,12,39], without considering the contribution from subsequent positive pressure phases and from the gas momentum flux. In this paper, we consider scaling for incident positive phase pressure impulse as well as for the total impulse. For the total impulse, we consider all the positive overpressure phases, i.e., not only from the phase corresponding to the incident/primary blast wave.

Using the same cube-root scaling law identified earlier [6], the scaled incident positive phase pressure impulse and the scaled total impulse as a function of the scaled distance are compared in Fig. 6. At scaled radius around 0.3 m $(\mathrm{kg})^{-1/3}$, the incident positive phase pressure impulse is lower than at radial distances immediately outwards for the three explosives considered. This is because this region ($\sim$ 0.3 m $(\mathrm{kg})^{-1/3}$) is contained within the distance that the secondary shock moves during its initial outward passage. The secondary shock gives rise to an early termination of the positive-phase duration of the pressure, thus explaining the

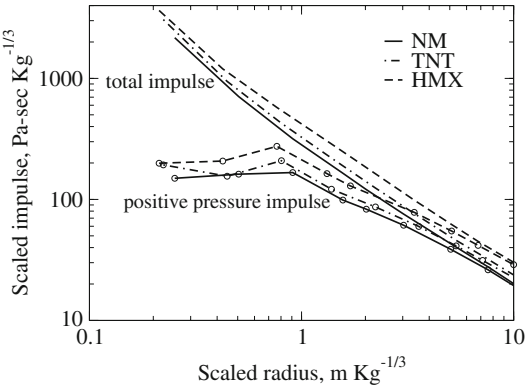

Fig. 6 Scaled impulse as a function of the scaled radius for NM, TNT and HMX

low-positive pressure impulse at scaled radius around 0.3 m $(\mathrm{kg})^{-1/3}$. At scaled radius around 0.8 m$(\mathrm{kg})^{-1/3}$, the incident positive-phase pressure impulse is observed to increase slightly for the three explosives considered. As pointed out earlier [39], the finite size of the explosive charge spreads out the energy, rather than concentrating it as a point source. Thus, the expanding detonation product gases tends to provide slightly increased pressure impulse. This trend in the pressure impulse has also been reported in a different study [12].

For the three explosives considered, the scaled total impulse decreases monotonically with scaled radius, due to the attenuation of the blast wave as it propagates outwards. The order of scaled impulse is HMX > TNT > NM, consistent with the order of their detonation energies. Empirical curve-fit for the shock overpressure, scaled incident positive phase pressure impulse, and scaled total impulse are obtained for the three explosives as a function of the scaled radius. We curve-fit overpressure (Δp), scaled incident positive pressure impulse (I_p) and scaled total impulse (I_t) using the following relations (a similar expression has been used elsewhere [38]):

$$\ln(\Delta p) = A_1 \ln(Z)^4 + B_1 \ln(Z)^3 + C_1 \ln(Z)^2 + D_1 \ln(Z) + E_1,$$

$$\ln(I_p/W^{1/3}) = A_2\ln(Z)^4 + B_2\ln(Z)^3 + C_2\ln(Z)^2 + D_2\ln(Z) + E_2, \quad (10)$$
$$\ln(I_t/W^{1/3}) = A_3\ln(Z)^4 + B_3\ln(Z)^3 + C_3\ln(Z)^2 + D_3\ln(Z) + E_3,$$

where Δp is expressed in MPa; I_p and I_t in Pa s, and W in kg. The variable Z denotes the scaled radius, $r/W^{1/3}$ in $\mathrm{m(kg)}^{-1/3}$. By curve-fitting the overpressure and impulse for the three explosives, we obtain the empirical constants in (10), and present them in Table 3. In order to ensure the independence of the scaling laws to the initial charge size, we consider different TNT charges comprising of 10,100, 1000, and 10,000 times the amount of TNT by mass as the baseline 11.8 cm dia charge (the case with 10,000 times corresponds to over 14 tons of TNT). These charges correspond to 0.2542, 0.5476, 1.18, and 2.542 m dia., respectively. Identical shock overpressure and scaled impulse are observed for all the TNT charges at the same scaled radius, thereby ensuring a wider applicability of the scaling laws proposed. Based on our experience, we must, however, emphasize that very near to the charge, slight dependence to the charge size exists; in particular, for scaled radius, $Z \sim 0.2\,\mathrm{m(kg)}^{-1/3}$ and less, the results are sensitive to the charge size. Hence, the scaling laws we have proposed are recommended for use only beyond $Z > 0.25\,\mathrm{m(kg)}^{-1/3}$.

A generalized empirical scaling law applicable for any explosive can be very useful in their design. To this end, we use the scaling laws for each explosive and curve-fit the coefficients with their respective detonation energies. Denoting E as the detonation energy of an explosive in MJ/kg, the coefficients A_1, B_1, etc. can be again curve-fit as functions of E as

$$A_1 = \lambda_{A_1}E^2 + \mu_{A_1}E + \delta_{A_1} \text{ etc.} \quad (11)$$

These new curve-fit coefficients (λ, μ, δ) are summarized in Table 4. Although we have chosen detonation energy as

Table 3 Overpressure scaling for the three explosives

Explosive	A_1	B_1	C_1	D_1	E_1	Range
NM	0.2656	0.2425	−0.5714	−2.2821	0.1383	0.25 < Z < 2.5
	0.1057	−0.7078	1.9499	−4.2259	0.6280	2.5 < Z < 10
TNT	0.0749	0.1981	−0.3841	−2.3607	0.3381	0.25 < Z < 2.5
	−0.0524	0.2543	−0.1017	−2.4808	0.2762	2.5 < Z < 10
HMX	−0.2121	−0.2847	−0.2725	−2.2089	0.5866	0.25 < Z < 2.5
	0.0982	−0.6876	2.0007	−4.4864	1.1907	2.5 < Z < 10

Table 4 Empirical scaling law for explosives

Coefficient	0.25 < Z < 2.5			2.5 < Z < 10		
	λ	μ	δ	λ	μ	δ
A_1	0.0714	−1.0457	3.4628	0.3114	−3.1841	8.0645
B_1	−0.2534	2.2377	−4.6971	−1.9119	19.5337	−49.5018
C_1	−0.1806	2.0417	−6.0356	4.1378	−42.2129	107.2791
D_1	0.2048	−2.0425	2.7274	−3.6608	37.2042	−96.7928
E_1	−0.1086	1.4059	−3.9221	1.0693	−10.5445	26.2635
A_2	−0.3467	3.6864	−8.8202	−0.0980	1.0888	−2.9745
B_2	−0.1405	1.8144	−4.5817	0.5245	−5.8600	16.1385
C_2	0.6748	−6.8822	16.2307	−0.9927	11.1687	−31.1728
D_2	0.1660	−1.8619	4.1698	0.7793	−8.8246	24.2358
E_2	−0.0619	0.8792	2.3976	−0.2217	2.7346	−3.1971
A_3	−0.0621	0.6813	−1.8305	0.3125	−3.1383	7.6995
B_3	−0.0521	0.5654	−1.5749	−1.9823	19.9721	−49.1849
C_3	0.0345	−0.4329	1.3566	4.4658	−45.1129	111.4637
D_3	0.0246	−0.2093	−0.7844	−4.2205	42.6989	−106.8735
E_3	−0.0256	0.5261	3.8357	1.3814	−13.7146	39.0919

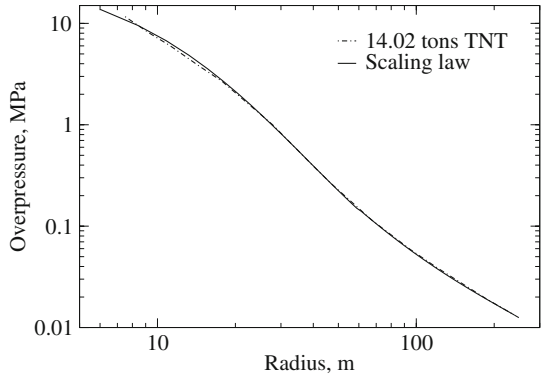

Fig. 7 Comparison of a 14.02 ton TNT charge with our scaling law

the variable for the curve-fit, other explosive parameters can also be used, for example, detonation velocity or Chapman-Jouguet pressure. More explosives can be considered, and the curve-fit coefficients (λ, μ and δ) can be fine-tuned if needed. To illustrate the significance of our scaling law, we simulate the blast from a 14.02 ton TNT charge and compare the overpressure with the scaling law that is proposed, presented in Fig. 7. The results are in good agreement, thus exemplifying the applicability of our scaling law for armaments, both kilo- and ton-range alike.

4.2 Effect of hydrodynamic instabilities

To study the effect of the growth of hydrodynamic instabilities in explosive blasts, we use a three-dimensional sector grid approach. However, to understand the applicability of this approach, we first undertake a simulation with the three-dimensional sector grid without any hydrodynamic instabilities for the baseline 11.8 cm dia NM charge. A spherical sector 12 m long, and 20° in the azimuth (θ) and zenith (ϕ) directions is considered, and a $5{,}000 \times 10 \times 10$ mesh is used. Free-slip boundary conditions are used along the sides of the sector and supersonic outflow in the outward plane. The initialization uses the same one-dimensional detonation profiles obtained from the GISPA method (Sect. 3.2). In Fig. 8a, we show the pressure traces at a radial location 0.9 m from the center of the charge based on the one-dimensional and three-dimensional simulations, and the results are in good agreement. This result demonstrates that the results with the sector grid and the 1D studies agree, which exemplifies the overall applicability of the approach. In Fig. 8b, the pressure contour is shown at time 3.34 ms after the detonation process, and the primary and secondary blast waves are observed to maintain a spherical shape. Other grid sizes and sector angles also show good agreement with the one-dimensional studies. The 20° sector is resolved with ten grid points in the lateral directions, i.e., corresponding to an azimuth/zenith angular cell increment, $\Delta\theta = \Delta\phi = 2°$. For very large sector grid cell increment angles ($\Delta\theta, \Delta\phi > 10°$), slight distortions from the spherical nature of the problem is observed, and thus, necessitates increase in resolution.

In order to better understand the effect of hydrodynamic instabilities in explosive blasts, we analyze a 11.8 cm dia TNT charge using a sector grid of size $1{,}000 \times 45 \times 45$. A spherical sector, 2.4 m long and 45° in the azimuth and zenith directions is used, and the one-dimensional detonation profiles (Sect. 3.2) are used for initializing the explosive charge. At the initial instant, the detonation products are assumed to be a mixture of N_2, H_2O, CO and C, with the initial mass fractions obtained from the chemical reaction

$$C_7H_5N_3O_6\ (\text{TNT}) \rightarrow 1.5N_2 + 2.5H_2O + 3.5CO + 3.5C. \tag{12}$$

Grids of sizes $1{,}000 \times 30 \times 30$ (G1), $1{,}000 \times 45 \times 45$ (G2), $1{,}000 \times 60 \times 60$ (G3), and $1{,}000 \times 75 \times 75$ (G4) have been tried. Comparing the time of arrival of the secondary shock, the mixing layer boundaries (to be defined shortly), and the mass-fraction of fuel remaining in the charge, we observe that the results with G2 only marginally differ from G1, and are in accordance with G3 and G4. Since the focus of this study is on these parameters, we conclude from these observations that G2 suffices; for the remainder of this paper, we present results with the G2 grid.

To help trigger the growth of instabilities, random fluctuations Gaussian or Laplace in nature are added to the density

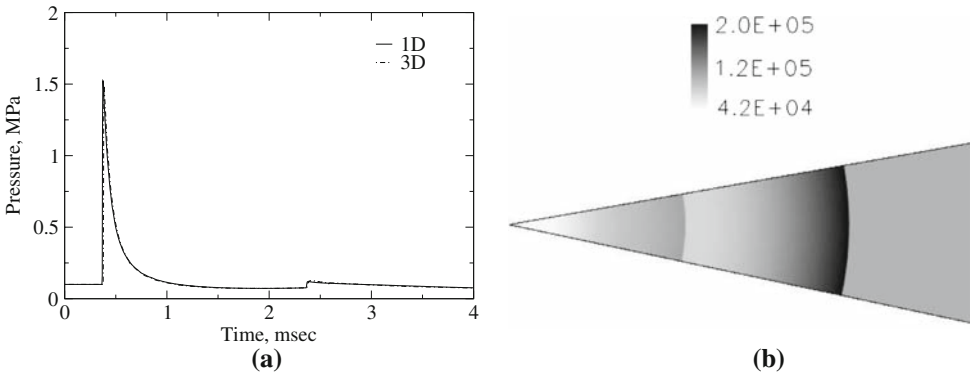

Fig. 8 Comparison of one-dimensional and three-dimensional approaches (**a**) pressure trace; (**b**) pressure contour

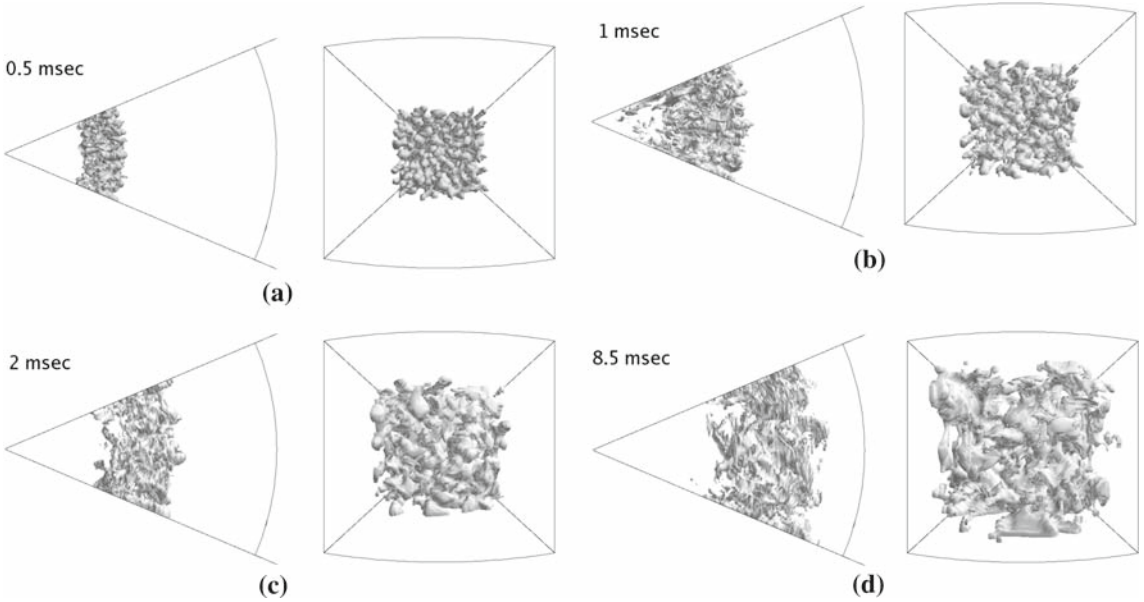

Fig. 9 Iso-surface of N_2 mass fraction to illustrate the growth of the mixing layer with time

(and energy) profiles in a radial sector region $0.9\,r_0 \leq r \leq r_0$, where r_0 denotes the initial charge radius. Other investigators [5,18] used similar perturbation procedures, albeit outside the charge. The source of these instabilities could be assumed to arise either from granular irregularities in the charge surface or from molecular fluctuations.

Figure 9 shows the mixing layer (iso-surface of N_2 mass fraction with value corresponding to mean of N_2 mass fraction in detonation products and ambient air) shape at four different times using the $1{,}000 \times 45 \times 45$ grid and Gaussian initial perturbation. During the initial blast wave phase, the structures grow in time, yet preserve their initial perturbation shape (0.5 ms, Fig. 9a). The mixing layer is created where the detonation products and the shocked air co-exist. Vorticity is created in the mixing layer, leading to entrainment of the surrounding air into these structures, resulting in their spatial growth, and afterburn/combustion between the detonation products (C and CO) and the shocked air. During the implosion phase, the secondary shock, as it implodes inwards, drags along with it the lower end of the mixing layer (1 ms, Fig. 9b). During the re-shock phase, the secondary shock passes through the mixing layer, which is a classic Richtmyer-Meshkov scenario, resulting in more vorticity creation due to baroclinic torque effects $(-\nabla(1/\rho) \times \nabla p)$. This results in interaction between contiguous structures, which in turn leads to further mixing enhancement in the layer as is evident from the profiles at 2 ms (Fig. 9c). Subsequently, in the asymptotic phase, contiguous structures begin to merge, thereby giving rise to a more distorted and wrinkled appearance to the mixing layer (8.5 ms, Fig. 9d). This merging between structures results in loss of memory of the initial perturbation shape. Thus, the problem under study is characterized by these four different phases, each being influenced by distinctly different fluid mechanics.

In order to quantitatively understand the growth of the mixing layer, we consider the spatially averaged N_2 mass fraction in the azimuth and zenith directions, and assume $1.05{Y_{N_2}}^i$ and $0.95{Y_{N_2}}^\circ$ to represent the inner and outer boundaries of the mixing layer, respectively, where ${Y_{N_2}}^i$ and ${Y_{N_2}}^\circ$ denote the nitrogen mass fraction in the detonation products and ambient air, respectively. Figure 10 shows the locus of the boundaries of the mixing layer. At early times (~0.5 ms), the inner and outer boundaries of the mixing layer are propagated outwards due to the outward motion of the blast wave. During the implosion phase (0.5–1 ms), the secondary shock drags the inner boundary of the mixing layer along with it, resulting in an increase of the mixing layer width (defined as the gap between the outer and inner boundaries). Subsequently, during the re-shock phase (1–2 ms), the outward-moving secondary shock drags along with it the inner boundary of the mixing layer, causing the mixing layer width to shrink. At around 3 ms, the inward-moving tertiary shock causes the inner boundary of the mixing layer to propagate inwards, albeit not as much as observed during the secondary shock's implosion. Furthermore, since the tertiary shock is weak, its contribution to the mixing layer width during its subsequent outward passage is not as pronounced as that of the secondary shock. This is followed by the asymptotic phase (>5 ms), during which, the overall width of the mixing layer slowly widens and asymptotes. Some of these features have also been reported [5].

Upon curve-fitting the mixing layer width with time, the growth is observed to be different during the different phases. During the blast wave phase, the growth is observed to be

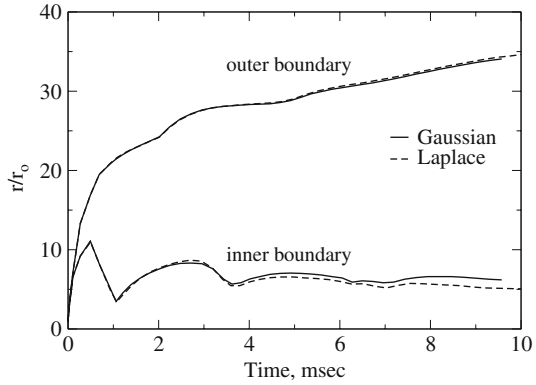

Fig. 10 Inner and outer boundaries of the mixing layer for the TNT charge

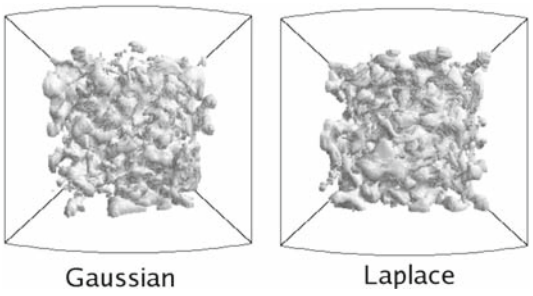

Fig. 11 Iso-surface of N_2 mass fraction at 3.2 ms for the random initialization based on Gaussian and Laplace distributions

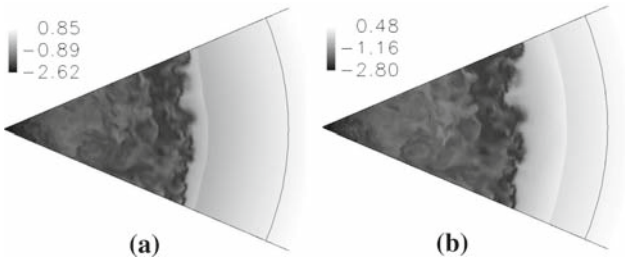

Fig. 12 Natural logarithm of density contours at (**a**) 2.25 ms; (**b**) 2.72 ms

linear, and given by the expression, $w/r_o = 7.4\left(t/W^{1/3}\right)$, where w denotes the mixing layer width based on the above definition, r_o denotes the initial charge radius, t is the time in ms, and W, the mass of the explosive in the charge in kg. For the implosion phase, the mixing layer width is observed to grow non-linear due to the inward stretching of the lower boundary of the mixing layer, and the curve-fit expression is found to be $w/r_o = 19.7\left(t/W^{1/3}\right)^{1.56}$. These expressions can be used to predict the early stages of the mixing layer growth with time.

Although we have used both Gaussian and Laplace distributions in the initialization to trigger the growth of instabilities in the region $0.9\,r_0 \leq r \leq r_0$, the mixing layer growth is nearly the same for both, as evident from Fig. 10. In both these scenarios, the initial perturbations grow to much larger sizes quickly, and thus the exact scale of the initial perturbation loses significance. Furthermore, after the re-shock phase, as observed in Fig. 9, contiguous structures interact and merge, thereby resulting in loss of memory. Due to this, the exact initial perturbation does not have a uniqueness to the later development and behavior of the flow field. However, the appearance of the fireball will be different for a different initial perturbation function, as shown in Fig. 11, where the iso-surface of the N_2 mass fraction is shown at 3.2 ms for the Gaussian and Laplace distribution based initial perturbation. As evident from the figure, the final appearance of the structures in the mixing layer is different for the Gaussian and Laplace distribution based initial perturbations. This has implications to real explosive blasts: two different charges of the same size and high explosive, upon detonation, can result in the same afterburn energy, pressure trace, and impulsive loading; however, the fireball will most certainly look different in photography. The imperfections on two real explosive charges will be different, and this will make their visual appearance different, as the structures evolve non-linearly with time.

As the secondary shock passes through the mixing layer, it interacts with the structures, giving rise to a classical Richtmyer-Meshkov instability, which is characterized by the creation of vorticity due to baroclinic effects. Due to this vorticity, the secondary shock distorts in shape. However, as the secondary shock propagates outside the mixing layer, as there are no more significant baroclinic effects, the secondary shock re-attains its spherical shape outside the mixing layer. To illustrate this fact, the natural logarithm of density (density in kg/m^3) contours are shown in Fig. 12 at 2.25 and 2.72 ms. At the earlier time, the secondary shock is distorted as it traverses through the mixing layer and just emerges out of the mixing layer, due to the presence of vortical structures arising from baroclinic effects. These structures cause spatially varying levels of afterburn/exothermicity, and thus spatially varying speeds of sound, causing the secondary shock to be faster in some regions, and slower in others. This creates the distorted shape of the secondary shock; however, within the next 0.47 ms, the secondary shock re-attains a spherical shape further outside the mixing layer, due to transverse pressure waves which tend to equalize pressure in the transverse directions.

During the asymptotic phase, the regions of exothermicity are predominantly confined to the regions where the C and CO in the detonation products mix with the ambient O_2. To illustrate this fact, the mass fraction of CO_2 and temperature contours are shown in Fig. 13 at 3.2 ms. As observed, the two contours peak near the outer boundary of the mixing layer, illustrating that combustion and exothermicity are confined

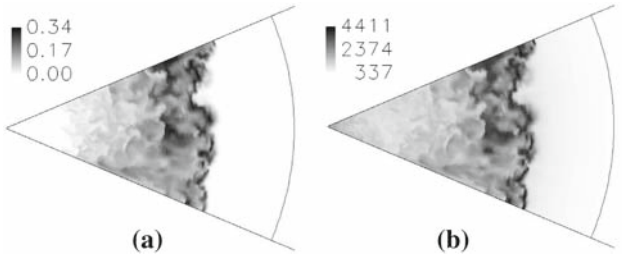

Fig. 13 Exothermicity at 3.2 ms (**a**) CO_2 mass fraction; (**b**) temperature (in K)

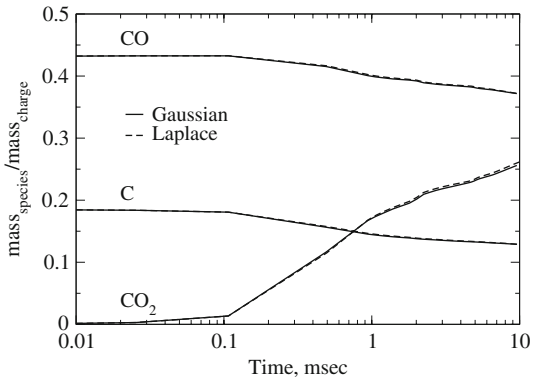

Fig. 14 Normalized mass of *CO*, *C* and CO_2 variation with time

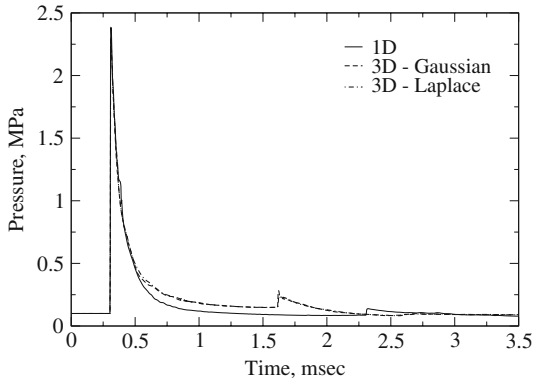

Fig. 15 Pressure traces at the 0.9 m radial location for the TNT charge

to where the fuel and oxygen mix. Furthermore, CO_2 acts as a blanket between the inner C and CO, and the outer O_2, resulting in the rate of burning/exothermicity being limited, and can only react any further if there is any turbulent mixing between the inner detonation products and the outer air. These observations may be different if the C and CO in the detonation products are assumed to also react with the H_2O, a process referred to as anaerobic burning. However, no reliable data exists in literature to quantify the occurrence and the precise amount of anaerobic burning behind explosive blast waves.

To better understand the rate of combustion/ afterburn, the time varying mass of CO, C and CO_2 are normalized with the initial charge mass and shown in Fig. 14. Since the chemical kinetic rates are assumed infinitely fast, by rate of combustion, we refer to the rate at which convective mixing-controlled combustion occurs, i.e., not from diffusion or chemical kinetics. The burning rates are sufficiently fast at early times (<1 ms) as the detonation products and shock-compressed oxygen interact for the first time. Subsequently, due to the presence of CO_2, which acts as a blanket between the detonation products and the shocked oxygen, the burning rate is slowed down. Thus, although more afterburn occurs during the asymptotic phase [18], the burning rate is slower than the corresponding rates at the earlier phases. It is due to this slow afterburning that the primary shock is almost unaffected by the afterburn energy release, as we will show in the next paragraph. These burning studies provide useful insights into how fast and how much of the detonation products burn, and the amount of exothermicity involved. Often, one-dimensional studies [40] investigate the blast problem with a parametric energy release, as the exact energy release can only be accurately deduced from three-dimensional studies. Thus, targeted 3D studies can be used to predict the accurate energy release, and can then be used in parametric one-dimensional studies.

To understand the effect of afterburn on impulsive loading, the pressure traces for the 1D and 3D studies for the same TNT charge are compared in Fig. 15 at 0.9 m from the charge center. The increased mixing and afterburn associated with the three-dimensional case is not observed to affect the primary shock, as the afterburn energy release occurs over a time frame of a few hundred milliseconds, which is not fast enough to couple with the primary shock. However, the secondary shock is observed to be slightly faster and stronger for the three-dimensional case, due to the increased afterburn energy release, which in turn results in lesser attenuation of the secondary shock as it traverses the mixing region. Another key observation is that the decay rate of the pressure profiles behind the primary shock is substantially different between the 1D and 3D cases. For instance, at around 1 ms, in the case with instabilities and enhanced mixing/afterburn (3D), the pressure decay is less than the corresponding 1D case. It appears that mixing and afterburn energy release is associated with three important features: (1) acceleration of the secondary shock; (2) stronger secondary shock, and (3) lesser decay rate of the pressure behind the primary shock. However, since the primary blast wave is nearly unaffected by the afterburn energy release, 1D studies will suffice for estimating the primary blast wave overpressure.

The dependence of the pressure on mixing and afterburn has implications in the impulsive loading estimation of explosive charges. The positive-phase incident pressure impulse and the total impulse for the 1D and 3D cases are

Table 5 Scaled impulse for TNT without (1D) and with (3D) mixing

Scaled radius ($mkg^{-1/3}$)	Positive pressure impulse ($Pa\,sec\,kg^{-1/3}$)			Total impulse ($Pa\,sec\,kg^{-1/3}$)		
	1D	3D-11.25°	3D-22.5°	1D	3D-11.25°	3D-22.5°
0.80	208.9	334.4	335.5	425.9	572.6	611.5
1.38	121.4	177.8	177.5	219.6	296.7	293.0

tabulated in Table 5, and a significant increase is observed for the 3D study, due to increased mixing and afterburn energy release. We denote as 3D-11.25° and 3D-22.5°, respectively, the quarter ($\theta = \phi = 11.25°$) and half ($\theta = \phi = 22.5°$) azimuth and zenith locations of the 45° sector. The positive-phase pressure impulse and total impulse are higher for the 3D by about 46–60% and 34–43%, respectively. While the positive pressure impulse is nearly the same at 3D-11.25° and 3D-22.5° azimuth/zenith locations, the total impulse is slightly different at the 0.80 m $kg^{-1/3}$ location, as this radial location is near the center of the mixing layer, where, the presence of vortical structures introduces significant three-dimensionality. Near to the core of the mixing layer, pressure waves can propagate laterally, trying to attain a 'pressure equilibrium' in the azimuth and zenith directions, thus explaining the almost same positive pressure impulse at 3D-11.25° and 3D-22.5°. However, near the core of the mixing layer, vortical structures cause significant density gradients, and thus, the total impulse (due to the dynamic pressure term) differs by about 7% between 3D-11.25° and 3D-22.5° in the mixing layer. The total impulse is observed to be nearly the same for 3D-11.25° and 3D-22.5° at the 1.38 m $kg^{-1/3}$ location, as this is near the outer periphery of the mixing layer, where transverse variations are minimal.

While 1D results can accurately predict the shock overpressure, 3D studies appear more suited to make accurate impulse estimations. Furthermore, in the blast studies of high explosives, other natural factors such as ambient humidity, density stratifications, and dust content are important parameters that can affect impulsive loading on structures, and to predict these effects will require 3D simulations. The current methodology appears to have the requisite capability to study some of these significant effects within a single simulation strategy. Future studies will address some of these effects.

5 Conclusions

The propagation of blast waves from different explosives is investigated using a new hybrid solver that captures both unsteady propagating strong shocks, and shear turbulence within a single formulation. Both 1D and 3D studies are conducted to investigate the blast characteristics of explosives. Several validation studies are conducted to first demonstrate the accuracy of the hybrid solver. Subsequently, simulations using 1D analysis are used to study the scaling of the shock overpressure, incident positive phase pressure impulse, and the total impulse for the three explosives considered. A generalized empirical scaling law based on detonation energy content is presented, that may be useful for explosive design.

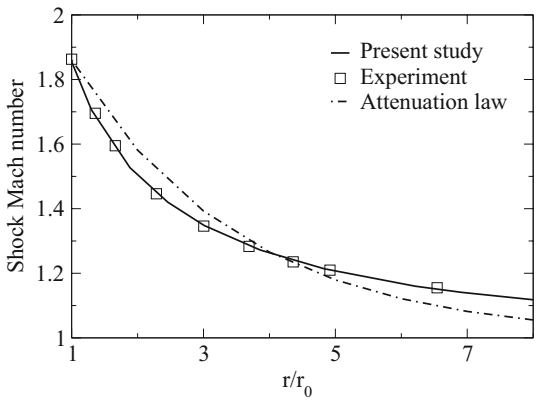

Fig. 16 Explosion from a pressurized sphere. Experimental data from [41]; Attenuation law from [42]

A key effort here has been to contrast 1D and 3D studies, especially the growth of 3D instabilities, and the associated mixing and afterburn. The growth of hydrodynamic instabilities is investigated, and mixing between the detonation products and the shock-compressed air is observed. Four distinctive phases of interest are observed, consistent with past studies. The mixing between the detonation products and the shock-compressed air is observed to result in afterburn energy release, which is found to affect the impulsive loading from the explosive charge. The impulse with mixing and afterburn is more pronounced in the 3D study, thus emphasizing the necessity for multidimensional studies for characterization of blast effects from explosives. Furthermore, mixing and afterburn are observed to significantly introduce a 3D dependence to the total impulse in regions within the mixing layer. Thus, it appears that while 1D studies may suffice for peak blast wave overpressure estimation, 3D physics must be resolved to obtain accurate characterization of impulsive loading from explosives.

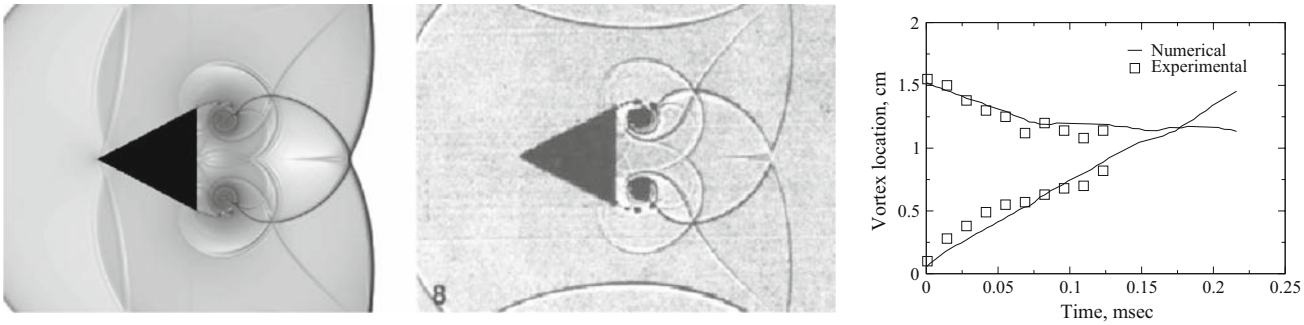

Fig. 17 (**a**) Numerical and (**b**) Experimental flowfields for the shock/wedge interaction problem; (**c**) time evolution of the vortex location

Acknowledgments This research was supported by the Office of Naval Research, the Air Force Office of Scientific Research and the Eglin Air Force Base. Simulations were performed at the Naval Oceanographic Office and U.S. Army Research Laboratory Major Shared Resource Center. The first author acknowledges the brief private communications with Dr. Allen Kuhl of the Lawrence Livermore National Laboratory.

Appendix A

In the first study, we focus on the attenuation of a shock wave from a pressurized sphere. Experimental and numerical investigations of the explosion of pressurized glass spheres were undertaken by Boyer [41]. Glass spheres of 5.08 cm dia., initially pressurized to 22 atm, are studied and the shock trajectory is tracked. A 1D grid 25.4 cm long with 7,500 grid points is considered (other grid sizes also provide the same result) with geometric source terms, and the calorically perfect gas model is used. Figure 16 shows the shock wave Mach number as a function of radial distance, normalized with the initial radius (r_o). The shock attenuation rate is also compared to the general attenuation law proposed by Aizik et al. [42] and good agreement is observed.

In the next study, the *Schardin's problem*, as reported by [43] is considered and simulated. The problem is that of a $M_s = 1.3$ traveling shock interacting with a 3-cm-long, 55° wide wedge. Due to the symmetry of the problem, only one half of the simulation domain is considered. The left plane is assumed to be an inflow; outflow boundary conditions are imposed on the top and right planes, and no-flux boundary condition for the surface of the wedge. We use a 850×300 grid for the present study, and this resolution is found to be sufficient to capture the underlying physical features. When the shock wave interacts with the wedge, it initially creates a triple point that links the moving shock, a contact discontinuity and a Mach stem that propagates along the wedge's wall. The diffraction of these Mach stems creates vortices on each side of the wedge that later interact with the diffracted waves. Comparison between experimental (image taken from [43]) and numerical flow fields is shown in Fig. 17. The numerical simulation captures the vortex generation and all subsequent wave interactions and generations. Consequently, the trajectory of the top vortex' center (with respect to the center of the base of the wedge) is correctly captured. The mainly linear evolutions only change in direction when interacting with the traveling waves. The experimental variations are attributed to the difficulty in locating the vortex centers from instantaneous Schlieren images. The present results for the vortex trajectory are in good agreement with the data [43], hence showing the low dissipation and high accuracy of the present simulation method.

References

1. Taylor, G.I.: The instability of liquid surfaces when accelerated in a direction perpendicular to their planes. Proc. R. Soc. Lond. A Math. Phys. Sci. **201**(1065), 192–196 (1950)
2. Brode, H.L.: Blast wave from a spherical charge. Phys. Fluids **2**, 217–229 (1959)
3. Richtmyer, R.D.: Taylor instability in a shock acceleration of compressible fluids. Commun. Pure Appl. Math. **13**, 297–319 (1960)
4. Kuhl, A.L.: Lawrence Livermore National Laboratory, Private Communication (2008)
5. Kuhl, A.L.: Spherical Mixing Layers in Explosions, Dynamics of Exothermicity. pp. 291–320. Gordon and Breach Publishers, Longhorn (1996)
6. Baker, W.E.: Explosions in Air. University of Texas Press, Austin (1973)
7. Wharton, R.K., Formby, S.A., Merrifield, R.: Airblast TNT equivalence for a range of commercial blasting explosives. J. Hazard. Mater. **79**, 31–39 (2000)
8. De Young, L.V., Campanella, G.: A study of blast characteristics of several primary explosives and pyrotechnic compositions. J. Hazard. Mater. **21**, 125–133 (1989)
9. Hargather, M.J., Settles, G.S.: Optical measurement and scaling of blasts from gram-range explosive charges. Shock Waves **17**, 215–223 (2007)
10. Vanderstraeten, B., Lefebvre, M., Berghmans, J.: A simple blast wave model for bursting spheres nased on numerical simulation. J. Hazard. Mater. **46**, 145–157 (1996)
11. Beshara, F.B.A.: Modelling of blast loading on aboveground structures—I. General phenomenology and external blast. Comput. Struct. **51**(5), 585–596 (1994)

12. Borgers, J.B.W., Vantomme, J.: Towards a parametric model of a planar blast wave created with detonating cord. In: 19th International Symposium on the Military Aspects of Blast and Shock, Calgary, Canada (2006)
13. Clutter, J.K., Mathis, J.T., Stahl, M.W.: Modeling environmental effects in the simulation of explosion events. Int. J. Impact Eng. **34**, 973–989 (2007)
14. Youngs, D.L.: Numerical simulation of turbulent mixing by Rayleigh-Taylor instability. Physica **12**, 32–44 (1984)
15. Brouillette, M.: The Richtmyer-Meshkov instability. Annu. Rev. Fluid Mech. **34**, 445–468 (2002)
16. Anisimov, S.I., Zeldovich, Y.B.: Rayleigh-Taylor instability of boundary between detonation products and gas in spherical explosion. Pis'Ma Zh. Eksp. Teor. Fiz. **3**, 1081–1084 (1977)
17. Anisimov, S.I., Zeldovich, Y.B., Inogamov, M.A., Ivanov, M.F.: The Taylor instability of contact boundary between expanding detonation products and a surrounding gas. Prog. Astronaut. Aeronaut. **87**, 218–227 (1983)
18. Kuhl, A.L., Ferguson, R.E., Oppenheim, A.K.: Gasdynamic model of turbulent exothermic fields in explosions. Prog. Astronaut. Aeronaut. **173**, 251–261 (1997)
19. Dobratz, B.M.: LLNL Handbook of Explosives, UCRL-52997. Lawrence Livermore National Laboratory, Livermore (1985)
20. Zukas, J.A., Walters, W.P.: Explosive Effects and Applications. Springer, Berlin (1997)
21. Hill, T.L.: An Introduction to Statistical Thermodynamics. Addison-Wesley, Reading (1960)
22. Johnston, I.A.: The Noble-Abel equation of state: thermodynamic derivations for ballistics modelling. Defence Science and Technology Organisation, DSTO-TN-0670 (2005)
23. Gordon, S., McBride, B.J.: Computer program for calculation of complex chemical equilibrium compositions and applications: I. Analysis. NASA Reference Publication 1311, Cleveland (1994)
24. Glaister, P.: An approximate linearized Riemann solver for the Euler equations for real gases. J. Comput. Phys **74**, 382–408 (1988)
25. Leveque, R.J.: Finite volume methods for hyperbolic problems. Cambridge University Press, Cambridge (2002)
26. Toro, E.F.: Riemann Solvers and Numerical Methods for Fluid Dynamics. Springer, Berlin (1999)
27. Neslon, C.: Simulations of spatially evolving compressible turbulence using a local dynamic subgrid model. PhD Thesis, Georgia Institute of Technology (1997)
28. Bdzil, J.B., Stewart, D.S., Jackson, T.L.: Program burn algorithms based on detonation shock dynamics: discrete approximations of detonation flows with discontinuous front models. J. Comput. Phys. **174**, 870–902 (2001)
29. Zhang, F., Frost, F.D., Thibault, P.A., Murray, S.B.: Explosive dispersal of solid particles. Shock Waves **10**, 431–443 (2001)
30. Xu, S., Aslam, T., Stewart, D.S.: High resolution numerical simulation of ideal and non-ideal compressible reacting flows with embedded internal boundaries. Combust. Theory Model. **1**, 113–142 (1997)
31. Lambert, D.E., Stewart, D.S., Yoo, S., Wescott, B.L.: Experimental validation of detonation shock dynamics in condensed explosives. J. Fluid Mech. **546**, 227–253 (2006)
32. Hayes D.B.: A $P^n t$ detonation criterion from thermal explosion theory. In: Sixth International Symposium on Detonation, Pasadena, CA (1976)
33. Xu, S., Stewart, D.S.: Deflagration-to-detonation transition in porous energetic materials: a comparative model study. J. Eng. Math. **31**, 143–172 (1997)
34. Massoni, J., Saurel, R., Lefrancois, A., Baudin, G.: Modeling spherical explosions with aluminized energetic materials. Shock Waves **16**, 75–92 (2006)
35. Youngs, D.L., Williams, R.: Turbulent mixing in spherical implosions. Int. J. Numer. Methods Fluids **56**, 1597–1603 (2008)
36. Pickard, W.F.: Base to apex thermal conductance of a cone embedded in a non-ideal insulator. Int. J. Heat Mass Transf. **47**, 5271–5283 (2004)
37. Menon, S., Patel, N.: Subgrid modeling for simulation of spray combustion in large-scale combustors. AIAA J. **44**(4), 709–723 (2006)
38. Department of defense ammunition and explosives hazard classification procedures. TB 700-2 NAVSEAINST 8020.8B TO 11A-1-47 DLAR 8220.1 (1998)
39. Kinney, G.F., Graham, K.J.: Explosive Shocks in Air. Springer, New York (1985)
40. Ames R.G., Drotar J.T., Silber J., Sambrook J.: Quantitative distinction between detonation and afterburn energy deposition using pressure-time histories in enclosed explosions. In: Thirteenth International Detonation Symposium, Norfolk, VA (2006)
41. Boyer, D.W.: An experimental study of the explosion generated by a pressurized sphere. J. Fluid Mech. **9**, 401–429 (1960)
42. Aizik, F., Ben-Dor, G., Elperin, T., Igra, O.: General attenuation laws for spherical shock waves in pure and dusty gases. AIAA J. **39**, 969–971 (2001)
43. Sivier, S., Loth, E., Baum, J., Löhner, R.: Vorticity produced by shock wave diffraction. Shock Waves **2**, 31–41 (1992)